Inorganic Chemistry
Article
pubs.acs.org/IC

Disorder−Order Structural Transformation in Electron-Poor $Sr_3Au_8Sn_3$ Driven by Chemical Bonding Optimization

Qisheng Lin, Jordan Vetter, and John D. Corbett*

Department of Chemistry, Iowa State University, Ames, Iowa 50011, United States

Supporting Information

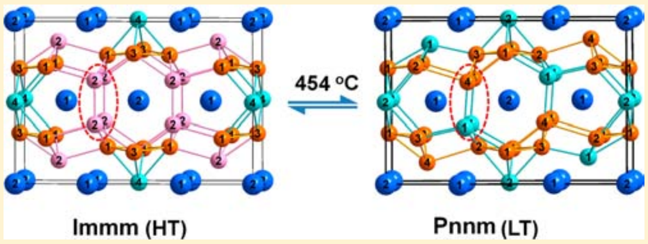

ABSTRACT: $Sr_3Au_8Sn_3$ was synthesized through fusion of a stoichiometric amount of pure metals at 800 °C and annealing treatments at lower temperatures. Single-crystal X-ray diffraction analyses revealed that $Sr_3Au_8Sn_3$ has a La_3Al_{11}-type *Immm* structure (a = 4.6767(8) Å, b = 9.646(2) Å, c = 14.170(2) Å, Z = 2) if annealed at 550 °C and above but a $Ca_3Au_8Ge_3$-type structure (*Pnnm*, a = 9.6082(8) Å, b = 14.171(1) Å, c = 4.6719(4) Å, Z = 2) if annealed at 400 °C. The transition occurs at about 454 °C according to DTA data. Both structures feature columns of Sr-centered pentagonal and hexagonal prisms of Au and Sn stacked along the respective longest axial directions, but different "colorings" of the polyhedra are evident. In the high-temperature phase (*Immm*) all sites shared between the two prisms adopt 50:50 mixtures of Au/Sn atoms, whereas in the low-temperature phase (*Pnnm*) Au or Sn are completely ordered. A *Klassengleiche* group−subgroup relationship was established between these two structures. LMTO-ASA calculations reveal that ΔE for the disorder-to-order transformation on cooling is driven mainly by optimization of the Au−Au and Au−Sn bond populations around the former mixed Au/Sn sites, particularly those with extremely short bonds at the higher temperature. These gains also overcome the smaller effect of ordering on the entropy decrease.

INTRODUCTION

Polar intermetallic phases containing a majority of gold have attracted increased interest in the field of solid state chemistry.[1] Discoveries of Au-rich polar intermetallics challenge our current conceptual models for rationalizing crystal structural and bonding. Generally speaking, polar intermetallics are electronically positioned between Zintl phases and the Hume−Rothery phases. However, the rules or concepts (such as the Wade−Mingos and Zintl−Klemm rules) developed for more ionic Zintl phases[2] no longer apply for Au-rich polar intermetallics[3] because of the existence of more bonds (>4) around each Au (a result of the relativistic effects in gold[4]) and the lack of deltahedral clusters in the latter phases. On the other hand, crystalline approximants of the respective icosahedral quasicrystals for a small number of Au-rich polar intermetallic phases, e.g., $Ca(Au,T)_{\sim 6}$ and $Ca_{\sim 13}(Au,T)_{\sim 76}$ (T = Ga,[5] In,[6] Ge,[7] Sn[8]), can be rationalized with the Hume−Rothery mechanisms.[9−11] However, in more cases, applications of the Jones Zone theory[10] (core of the Hume−Rothery mechanisms) to Au-rich polar intermetallics are disfavored; rather, complicated interplays among electronic, size, bonding, Madelung energy contributions (packing factors), chemical pressure, etc. terms give sound explanations.[12−15]

The La_3Al_{11}-type structure is apparently such a complicated system that no single rule or mechanism can explain all phenomena related to the La_3Al_{11} family members. Chemical bonding analyses within the anionic network of the parent La_3Al_{11} have suggested that this structural type can accommodate valence electron counts (vec) of ca. 38−42 e^-/fu.[16] The latter explains the existence of about 70 ternary phases with the common formula of $R_3M_xT_{11-x}$ (R = trivalent rare-earth metal; M = group 8−12 metals, $x \approx 1.5-4.5$; T = Al, Ga).[17] However, a number of electron-poorer examples with vec ≤ 30 have also been reported, e.g., R_3Zn_{11},[17] K_3Hg_{11},[18] and $Yb_3Au_{4.7}Ga_{6.3}$,[19] that indicate an increased influence of other than straightforward electronic factors. The influences of subtle changes of size and vec in La_3Al_{11}-type and related structures are particularly manifested in electron-poor (vec/atom < 2.2; one valence electron for Au) Au-dominated systems, $Ca_3Au_xGe_{11-x}$ ($x \approx 7-8$).[13] Recently, we established that the Au-richer phase $Ca_3Au_xGe_{11-x}$ ($x > 7.5$) forms with centric *Pnnm* symmetry, but a slight decrease of the Au/Ge ratio (or increase of vec) results in formation of the Au-poorer 3:11 phase $Ca_3Au_xGe_{11-x}$ ($x < 7.5$) with noncentric *Imm*2 symmetry. However, size factors are also prominent for this Au-rich phase, as evidenced by the experimental observations that replacement of Ca by Sr results in formation of $SrAu_3Ge$ ($P4/nmm$),[20] replacement of Ge by Ga leads to $Ca_3Au_{6.6}Ga_{4.4}$ ($P6_3/mmc$),[21] neither being an La_3Al_{11} type, and replacement of Ge by Sn yields $Ca_{14}Au_{45}Sn_6$ ($P6/m$),[22] a $Gd_{14}Ag_{51}$-type product.

In this work, we report the synthesis, structures, and bonding of $Sr_3Au_8Sn_3$ phases in the Sr−Au−Sn system, motivated by the biphasic separation of $Ca_3Au_xGe_{11-x}$ at different Au/Ge ratios.[13] Also, there are only two known ternary compounds in the Sr−Au−Sn system, i.e., the CaAuGe-type SrAuSn[23]

Received: March 13, 2013
Published: May 16, 2013

Table 1. Selected Reactions, Conditions, Products, and Lattice Constants for $Sr_3Au_8Sn_3$ Refined from Powder Data

			lattice constants from powder data[b]			
$Sr_3Au_{11-x}Sn_x$, x =	annealing temp. (°C)	products and their estimated yields[a]	a (Å)	b (Å)	c (Å)	V (Å^3)
4	400	25% *Pnnm* + 25% SrAuSn + 50% U1				
3.5	400	50% *Pnnm* + 20% SrAuSn + 30% U1	9.6164(6)	14.168(1)	4.6690(3)	636.14(5)
3	400	pure *Pnnm*	9.6113(6)	14.170(1)	4.6737(3)	636.51(5)
3	550	pure *Immm*	4.6656(3)	9.6234(6)	14.146(1)	635.14(5)
3	650	60% *Immm* + 40% SrAuSn	4.6666(3)	9.6587(7)	14.093(1)	635.20(5)
2.5	400	70% *Pnnm* + 30% SrAuSn	9.6007(6)	14.176(1)	4.6704(3)	635.64(5)
2	400	40% *Pnnm* + 30% $SrAu_5$ + 30% $SrAu_2$	9.6031(6)	14.177(2)	4.6719(5)	636.04(7)

[a] *Pnnm* and *Immm* denote the LT and HT forms of $Sr_3Au_8Sn_3$. Yields were roughly estimated from intensities of the strongest peaks in powder X-ray diffraction data. U1 denotes an unidentified phase. [b] Lattice constants of primary phase were refined from diffraction peaks that can be distinguished from those of other phases within 10−70° in 2θ.

(*Pnma*) and the $ThCr_2Si_2$-type $SrAu_{1.35}Sn_{2.65}$ (*I*4/*mmm*).[15] Interestingly, the structure of $Sr_3Au_8Sn_3$ does not accommodate varied compositions, in contrast to $Ca_3Au_xGe_{11-x}$;[13] rather, a disorder−order transformation driven by chemical bonding optimization occurs as a function of temperature.

■ EXPERIMENTAL SECTION

Syntheses. Starting materials are dendritic Sr metal pieces (99.95%, Alfa Aesar) with surfaces manually cleaned by a surgical blade, as-received Au particles (99.999%, BASF), and Sn shot (99.99%, Alfa Aesar). A stoichiometric amount of mixtures was put into precleaned Ta tubes ($\phi \approx 0.9$ cm) with one end previously weld sealed; then the other ends of the Ta tubes were crimped in the glovebox. All manipulations were made in an argon-filled glovebox ($H_2O < 0.1$ ppmv). After transferring into an arc welder, the other ends of the Ta tubes were weld sealed under argon, and finally, all Ta containers were enclosed in evacuated SiO_2 jackets ($<10^{-5}$ Torr).

$Sr_3Au_8Sn_3$ crystals were first isolated from a nominal composition of $SrAu_3Sn$ that was reacted at 800 °C for 6 h, quenched in water, annealed at 400 °C for 1 week, and quenched into water again. After the composition was established by single-crystal structural determination, stoichiometric reactions with common formula $Sr_3Au_{11-x}Sn_x$ (x = 2.0, 2.5, 3.0, 3.5, 4.0) were reacted to check the phase homogeneity range under the same conditions. Separate annealing treatments of $Sr_3Au_8Sn_3$ at 400, 550, and 650 °C followed by quench were also carried out to study phase transformation as a function of temperature.

Phase Analyses. These were performed on the basis of powder diffraction data collected by a STADI P powder diffractometer equipped with Cu $K\alpha_1$ radiation (λ = 1.540598 Å). Si standard (NIST 640c) was added to each sample for peak position calibration. The detection limit of a second phase for this system is conservatively estimated to be about 5 vol % in equivalent scattering power. Phase identification was done with the aid of PowderCell,[24] and lattice constants were refined with the aid of the program UnitCell[25] from diffraction peaks between 15° and 70° in 2 theta that are distinguishable from peaks of other phases. Table 1 lists the phase analysis results for each loaded reaction.

Thermal Analyses. Thermal analyses of a 91.6 mg $Sr_3Au_8Sn_3$ sample annealed at 400 °C were performed under an argon atmosphere on a Perkin Elmer Differential Thermal Analyzer (DTA-7). Samples were typically heated from room temperature to 1000 °C at a rate of 10 °C/min, kept at this temperature for 10 min, and cooled to 200 °C at the same rate. Powder patterns before and after DTA scans were recorded and are shown in Figure S1, Supporting Information.

Structural Determination. Single crystals isolated from nominal $Sr_3Au_8Sn_3$ samples annealed at 400, 550, and 650 °C and quenched and one that was directly quenched from 800 °C were selected for structural determination. Room-temperature intensity data were collected with the aid of a Bruker APEX CCD single-crystal diffractometer equipped with graphite-monochromatized Mo $K\alpha$ (λ = 0.71069 Å) radiation in an ω scan method over $2\theta = \sim 7-57°$. Data integration, Lorentz polarization, and empirical absorption corrections were made by means of the SMART software package.[26] Absent reflection analyses revealed that $Sr_3Au_8Sn_3$ annealed at 400 °C had space group *Pnnm*, whereas those annealed at 550 and 650 °C and the one directly quenched from 800 °C had *Immm* symmetry. Hence, in the following *Pnnm* and *Immm* phases are referred as low-temperature (LT) and high-temperature (HT) phases, respectively. Since crystals annealed at 550 and 650 °C and the one directly quenched from 800 °C gave the same space group, the same composition, and essentially the same atomic coordinates (according to the 3σ rule of thumb), only the result for the crystal annealed at 550 °C is reported here.

Solutions for both LT and HT $Sr_3Au_8Sn_3$ structures were quite straightforward; direct methods for each yielded all independent atomic sites. Assignments of Sr, Au, Sn, and/or Au/Sn mixtures were made on the basis of bond distances to respective neighboring atoms and isotropic displacement parameters. For the LT phase, four independent sites were found exclusively occupied by Au, two by Sn, and an additional two by Sr. In comparison, in the HT phase two sites were found exclusively occupied by Au, one by Sn, two by Sr, and one by a Au:Sn mixture with an ratio of 50:50(1)%. Separate refinements with isotropic displacement parameters were also made to check occupancies of all other atoms, but all resulting occupancy parameters were close to the unity, 0.99 (2)−1.02(2), suggesting no significant mixings or partial occupancies. Final least-squares refinements, with anisotropic displacement parameters and secondary extinction corrections, yielded R1= 3.61%, wR2 = 8.72%, and GOF = 1.096 for 46 parameters refined from 863 observed independent data for the LT phase (*Pnnm*) and R1= 3.47%, wR2 = 7.83%, and GOF = 1.081 for 29 parameters refined from 454 observed independent data for the HT phase (*Immm*).

Crystal and structural refinement data for LT and HT forms of $Sr_3Au_8Sn_3$ are listed in Table 2. Atomic coordinates for both standardized by STRUCTURE TIDY[27] are given in Table 3, together with site symmetry, occupancies, and isotropic displacement parameters, etc. Some important interatomic distances for both forms are given in Table 4.

LMTO-ASA Calculations. Seven models were considered as defect-free models for calculations for the HT structure, all subgroup symmetries of *Immm*. It turns out that these models, Figure S2, Supporting Information, can be described by *Pnnm*, *I*2*mm*, *Pmmm*, *Pmnm*, *Pnmm*, *Im*2*m*, and *I*2/*m* symmetries, and all have the composition $Sr_3Au_8Sn_3$. According to the calculations, the model with *I*2*mm* symmetry has the lowest total energy, the *Pnnm* model being the second, 0.23 eV higher in energy, whereas the others are all at least 0.6 eV higher than the latter. In the following, results of the lowest two models (*I*2*mm* and *Pnnm*) for HT structures are discussed in the text together with those of the LT structure.

Calculations were performed by means of the self-consistent, tight-binding, linear-muffin-tin-orbital (LMTO) method in the local density (LDA) and atomic sphere (ASA) approximations, within the framework of the DFT method.[28−30] ASA radii were scaled automatically at the default limit of 16% maximum overlap between two neighboring atomic spheres, and one interstitial sphere was

Table 2. Structural Data and Refinements for HT and LT Forms of $Sr_3Au_8Sn_3$

	HT	LT
formula	$Sr_3Au_{8.00(4)}Sn_{3.00(4)}$	$Sr_3Au_8Sn_3$
f.w.	2194.66	2194.66
space group	*Immm*	*Pnnm*
a (Å)	4.6767(8)	9.6082(8)
b (Å)	9.646(2)	14.171(1)
c (Å)	14.170(2)	4.6719(4)
vol. (Å^3)	639.2(2)	636.11(9)
Z	2	2
d_{calcd} (g/cm^3)	11.414	11.458
abs coeff (mm^{-1})	109.483	110.022
no. of reflns collected/R_{int}	1965/0.0461	5216/0.0625
data/restraints/params	454/0/29	863/0/46
GOF	1.081	1.096
R1/wR2 [$I > 2\sigma(I)$]	0.0347/0.0783	0.0361/0.0872
R1/wR2 (all data)	0.0434/0.0831	0.0389/0.0891
ext coeff	0.00050(8)	0.00052(9)
max/min peaks (e·Å^{-3})	2.544/−3.446	3.812/−2.780

inserted accordingly. Reciprocal space integrations were carried out by means of the tetrahedron method. The basis sets were 4d/5s/(5p) for Sr, 5d/(5f)/6s/6p for Au, and 5s/5p for Sn, with orbitals in parentheses down-folded. Scalar relativistic effects were included in the calculations. Band structures were calculated using 325 *k* points to sample Brillouin zones. Crystal orbital Hamilton population (COHP) analyses[31] were performed to gain insights into the bonding properties.

■ RESULTS AND DISCUSSION

Phase Stability and Phase Width. Figure 1 shows the experimental (black) and simulated (red) powder patterns for $Sr_3Au_8Sn_3$ annealed at (a) 400 and (b) 550 °C. Both experimental patterns show excellent agreement with the calculated patterns, indicating ≥95% pure phases were obtained. As shown, both patterns display similar distributions of reflection peaks, but the pattern for sample annealed at 400 °C exhibits several additional weak reflections at 2θ angles smaller than ca. 35°, which are indexed as (120), (221), (320), and (311) in *Pnnm* symmetry. On the contrary, $h + k + l = 2n + 1$ reflections are naturally absent in *Immm* symmetry. With these major differences, phase identification can be made for powder patterns of other products, see Table 1. According to experimental results, $Sr_3Au_8Sn_3$ always crystallizes in *Pnnm* symmetry if samples are annealed at 400 °C, but if the annealing temperature is raised to 550 °C (and above) and the sample quenched thereafter, the symmetry changes to *Immm*. This is consistent with the DTA results (Figure S1, Supporting Information), which show a phase transition at about 454 °C. In addition, $Sr_3Au_8Sn_3$ was always obtained as pure phase from a nominal composition ratio of Sr:Au:Sn = 3:8:3, but slight changes of the Au/Sn ratios (e.g., $x = 2.5$ and 3.5) resulted in the appearance of $SrAuSn$,[23] $SrAu_5$,[32] $SrAu_2$,[33] and other unknown phases.

According to the refined lattice constants, Table 1, the LT form of $Sr_3Au_8Sn_3$ (*Pnnm*) is not a line compound at 400 °C. However, its homogeneous composition range is expected to be narrow because of the small variations found, Δa = 0.0157(9) Å, Δb = 0.009(2) Å, Δc = 0.0047 (4) Å, with the largest deviation of 19σ in *a*. A narrow homogeneity range is also possible according to the COHP data, which change from bonding to antibonding character at the Fermi energy (below). Therefore, no effort has been made to refine compositions of single crystals selected from $x \neq 3$ loadings.

Group−Subgroup Relationship. The HT form of $Sr_3Au_8Sn_3$, space group *Immm*, belongs to the La_3Al_{11}-type structure. In this structure, there are two independent sites (Wyckoff 4f and 2d) for electropositive Sr atoms and four sites for electronegative atoms (a Wyckoff 8l (0 *y z*) site for Au1 and another for Au/Sn2 admixtures, a 4h (0 *y* 1/2) site for Au3, and a 2d (1/2 0 1/2) site for Sn4; see Table 3). In comparison, the LT form (*Pnnm*) has two sites (4i and 2a) occupied by Sr, four independent 4g sites for Au, and two (4g and 2b) for Sn. Figure 2 shows the detailed group−subgroup structural transformation between the HT and the LT structure types by means of a Bärnighausen tree.[34] A *Klassengleiche* group−subgroup relationship can be established between these two structures: Au1 at Wyckoff 8l site in *Immm* splits into two 4g sites (Au2 and Au3) in *Pnnm* symmetry; the Au/Sn2 mixture in 8l splits into another two 4g sites (Au4 and Sn1); Au3 and Sn4 correspond, respectively, to Au1 and Sn4 in *Pnnm*, and Sr1 and Sr2 in *Immm* also correspond to Sr1 and Sr2 in *Pnnm*.

Table 3. Crystallographic Data for HT and LT Forms of $Sr_3Au_8Sn_3$

atom[a]	Wyckoff	symmetry	*x*	*y*	*z*	U_{eq} (Å^2)
			Immm (HT)			
Au1	8n	m..	0	0.2804(1)	0.1301(1)	0.021(1)
M2	8n	m..	0	0.3647(1)	0.3358(1)	0.029(1)
Au3	4f	m2m	0	0.1973(1)	1/2	0.022(1)
Sn4	2b	mmm	1/2	0	1/2	0.017(1)
Sr1	4g	mm2	0	0	0.3036(2)	0.017(1)
Sr2	2a	mmm	0	0	0	0.023(1)
			Pnnm (LT)			
Au1	4g	..m	0.1972(1)	0.0020(1)	0	0.022(1)
Au2	4g	..m	0.2788(1)	0.3739(1)	0	0.021(1)
Au3	4g	..m	0.2822(1)	0.6339(1)	0	0.020(1)
Au4	4g	..m	0.3762(1)	0.1590(1)	0	0.022(1)
Sn1	4g	..m	0.6551(1)	0.1729(1)	0	0.016(1)
Sn2	2b	..2/m	0	0	1/2	0.018(1)
Sr1	4f	..m	0.0047(1)	0.1963(1)	0	0.017(1)
Sr2	2c	..2/m	0	1/2	0	0.022(1)

[a] M = 0.50(1) Au + 0.50(1) Sn.

Table 4. Important Interatomic Distances (Angstroms) for HT and LT Forms of $Sr_3Au_8Sn_3$[a]

bond	distance (Å)	bond	distance (Å)	bond	distance (Å)
		Immm (HT)[b]			
Au1−M2 × 2	*2.7682(8)*	Au3−M2 × 2	2.832(1)	Sr1−M2 × 2	**3.548(1)**
Au1−Sn4	2.8074(9)	Au3−Au1 × 4	*2.9850(6)*	Sr1−Sn4 × 2	3.635(1)
Au1−Au3 × 2	*2.9851(6)*	Au3−Sn4 × 2	*3.0149(9)*	Sr1−Au1 × 2	**3.656 (1)**
Au1−M2	3.027 (2)	Sn4−Au1 × 4	2.8073(9)	Sr2−Au1 × 4	**3.2734(9)**
M2−M2	2.609(3)	Sn4−Au3 × 4	*3.0149(9)*	Sr2−M2 × 8	3.547(1)
M2−Au1 × 2	*2.7682(8)*	Sr1−Au1 × 4	3.292(1)	Sr2−Au3 × 4	3.741(1)
M2−Au3	2.832(1)	Sr1−M2 × 4	3.328(2)		
M2−Au1	3.027 (2)	Sr1−Au3 × 2	**3.372(2)**		
		Pnnm (LT)			
Au1−Au4	2.8118(9)	Au4−Sn1	2.687(1)	Sr1−Au2 × 2	3.340(1)
Au1−Sn1	2.856(1)	Au4−Au3 × 2	*2.8103(5)*	Sr1−Au4 × 2	3.345(1)
Au1−Au2 × 2	*2.9672(5)*	Au4−Au1	2.8118(9)	Sr1−Sn1	**3.375(2)**
Au1−Au3 × 2	*2.9984(5)*	Au4−Au2	3.1864(9)	Sr1−Au1	**3.414(2)**
Au1−Sn2 × 2	*3.0077(5)*	Sn1−Au4	2.687(1)	Sr1−Au4	**3.608(1)**
Au2−Sn1 × 2	*2.7034(6)*	Sn1−Au2 × 2	*2.7034(6)*	Sr1−Sn2 × 2	3.633(1)
Au2−Sn2	2.7766(6)	Sn1−Au3	2.803(1)	Sr1−Au2	**3.643(1)**
Au2−Au1 × 2	*2.9672(5)*	Sn1−Au1	2.856(1)	Sr1−Au3	**3.659(1)**
Au2−Au4	3.1864(9)	Sn2−Au2 × 2	2.7766(6)	Sr2−Au2 × 2	**3.2195(7)**
Au3−Sn1	2.803(1)	Sn2−Au3 × 2	2.8252(7)	Sr2−Au3 × 2	**3.3097(7)**
Au3−Au4 × 2	*2.8103(5)*	Sn2−Au1 × 4	*3.0077(5)*	Sr2−Au4 × 4	3.4567(5)
Au3−Sn2	2.8252(7)	Sr1−Au3 × 2	3.230(1)	Sr2−Sn1 × 4	3.6986(9)
Au3−Au1 × 2	*2.9984(5)*	Sr1−Sn1 × 2	3.314(1)	Sr2−Au1 × 4	3.732(1)

[a] Italics denote interlayer distances, and bold numbers are the center-to-waist interatomic distances for Sr1-pentagonal prisms and Sr2-hexagonal prisms; see text. [b] M = 0.50(1) Au + 0.50(1) Sn in HT structure.

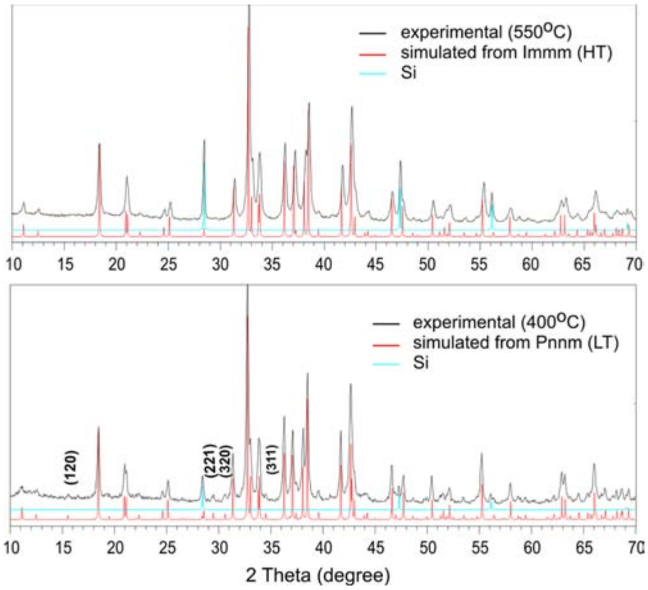

Figure 1. Experimental and calculated powder patterns for $Sr_3Au_8Sn_3$ annealed at 400 (bottom) and 550 °C (top). Indexes of some reflections at low angles that exist in *Pnnm* but not in *Immm* symmetry are marked.

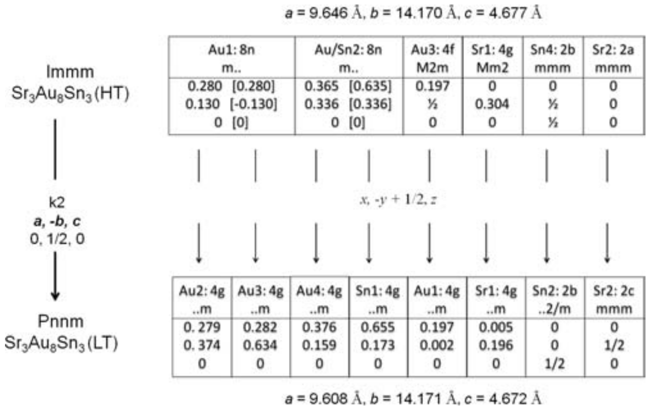

Figure 2. Bärnighausen tree for HT (*Immm*) and LT (*Pnnm*) structures of $Sr_3Au_8Sn_3$. Note the lattice constants and coordinates of the HT phase are transformed from the standard setting (Table 3) for comparison, and coordinates in brackets refer to symmetry-equivalent positions.

As with other La_3Al_{11}-type and derivative structures,[13,16] the present two structures may be viewed as vacancy ordered and structurally optimized 1 × 3 × 1 superstructures of the $BaAl_4$-type structure. Structural relationships between $BaAl_4$ and La_3Al_{11}-type structures have been well documented in the literature,[35] so only differences between HT and LT forms of $Sr_3Au_8Sn_3$ are discussed in the following.

Structure. Figure 3 shows the environments of the electropositive Sr1 and Sr2 atoms in both HT and LT forms. As shown in Figure 3a, Sr1 in the HT structure is encapsulated by a 16-atom polyhedron in which a subpolyhedron—a pentagonal prism defined by four Au1, four Au/Sn2 admixtures, and two Sn4 atoms—is highlighted as a yellow polyhedron. The 10 atoms that define each pentagonal prism are located on the front and back faces of the unit cell (cf. Figure 4); hence, no direct bonding interactions exist between atoms on the two pentagonal faces (separated by the lattice constant *a*). The remaining six atoms in the waist of each pentagonal prism (two Au1, two Au3, and two Au/Sn2) are located in a mirror plane at $x = 1/2$. However, these waist atoms are also vertices of neighboring pentagonal and hexagonal prisms displaced by $a/2$, and the waist-to-waist Au1−Au/Sn2 and Au3−Au/Sn2 bonds are edges of pentagonal and hexagonal faces (see Figure 4).

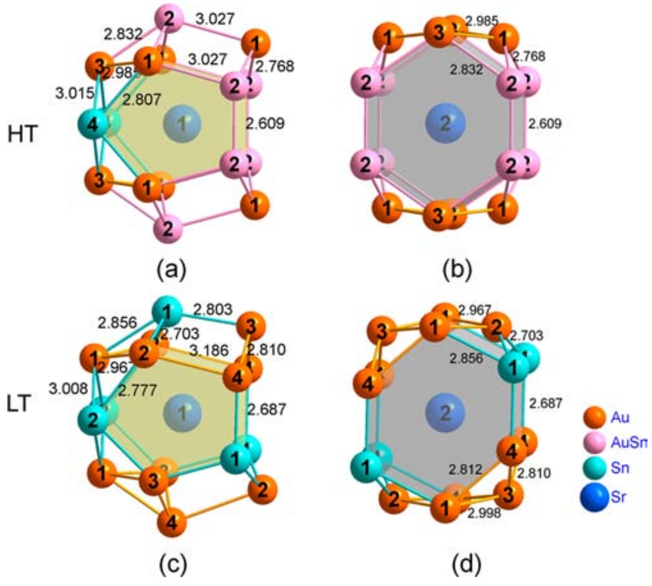

Figure 3. Environments of Sr1 and Sr2 in HT (a, b) and LT (c, d) forms of $Sr_3Au_8Sn_3$. Respective pentagonal and hexagonal prismatic polyhedra are shaded in yellow and gray. Numbers on spheres mark the atoms listed in Table 3, and small numbers are representative interatomic distances (Angstroms).

The neighboring atoms surrounding Sr2 in the HT structure also define a 16-atom polyhedron, consisting of four Au1 atoms, eight Au/Sn2 mixtures, and four Au3 atoms, but the 12 atoms sitting on the front and back faces of the unit cell define a hexagonal prism (shaded gray) viewed along the *a* axis, Figure 3b, and the four Au1 neighbors with the smallest distances to Sr2 (3.2734 (9) Å) cap the four heteroatomic rectangular faces of the hexagonal prism on the waist.

Similar coordination environments for Sr1 and Sr2 are found in the LT structure; however, distinctive differences in "coloring" are evident. The 16-atom Sr1-polyhedron is defined by 11 Au and five Sn atoms, Figure 3c. Of these, the six Au and four Sn with coordinates $z = 0$ or 1, that is, 2 Au2 + 2 Au3 + 2 Au4 + 2 Sn1 + 2 Sn2, form a pentagonal prism (yellow), leaving two Au1, one Au2, one Au3, and one Au4 as the capping atoms on the waist. Again, the last capping atoms are actually located on the pentagonal or hexagonal faces of neighboring prisms (see Figure 4). As to Sr2, the 16-atom polyhedron consists of 12 Au and 4 Sn atoms, of which 4 Au1, 4 Au4, and 4 Sn1 atoms define a hexagonal prism shaded in gray, with its waist capped by 2 Au2 and 2 Au3 atoms, Figure 3d. Note that the foregoing pentagonal and hexagonal prisms are simply shown as their projections; these should not imply that prism-to-Sr distances are shorter than the corresponding waist-to-Sr distances. Interatomic distances for each atom cluster are detailed in Table 4, in which atoms on the waists of Sr1-pentagonal prisms and Sr2-hexagonal prisms are highlighted with bold numbers. As can be seen, the waist-to-Sr distances for the Sr2-centered hexagonal prisms are always less than the prism-to-Sr distances; a similar situation exists for some distances within the Sr1-pentagonal prisms. An easier correlation for the effects of HT versus LT types on distances can also be seen in Figure 3.

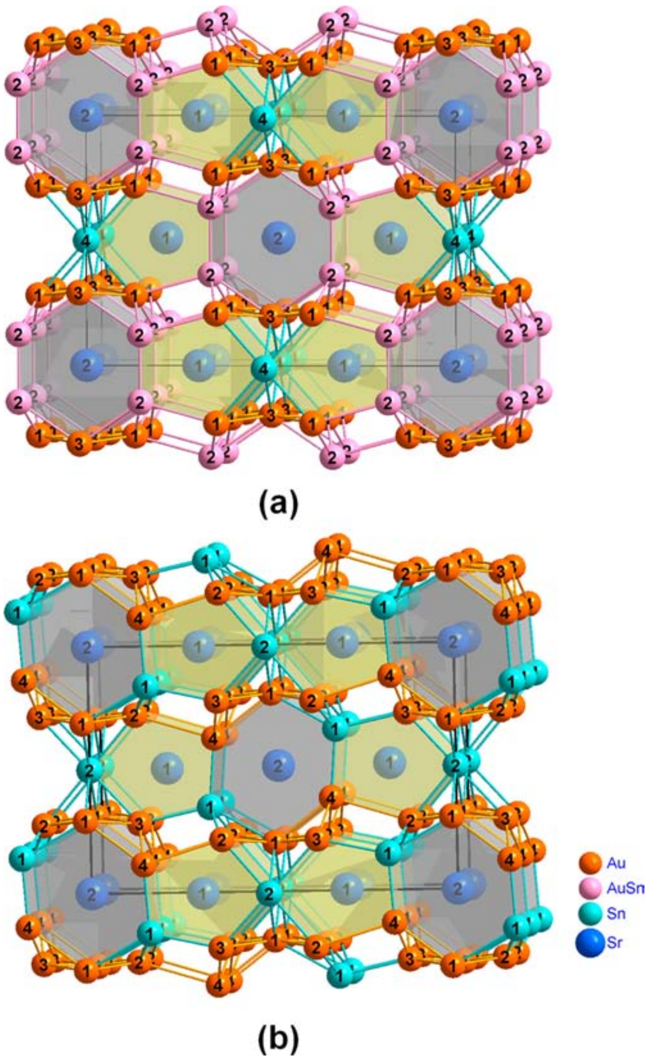

Figure 4. Unit cells of $Sr_3Au_8Sn_3$ with (a) *Immm* (HT) and (b) *Pnnm* (LT) symmetries. Numbers on spheres mark the atoms as listed in Table 3. Origin for the LT form (*Pnnm*) is shifted to (0 1/2 0).

Figure 4 shows the three-dimensional condensation of the foregoing 16-atom polyhedra of Sr1- and Sr2-centered clusters in unit cells of (a) HT and (b) LT forms of $Sr_3Au_8Sn_3$ along respective short axial directions, i.e., (100) for HT form and (001) for LT. Both cells exhibit the same long-range order in terms of the Sr1- and Sr2-centered clusters. If only the Sr1-pentagonal and Sr2-hexagonal prisms are considered, both structures can be viewed as stacking of polyhedral layers. For the HT structure, Sr1-pentagonal and Sr2-hexagonal prisms are condensed into infinite columns extending along the *a* direction through shared pentagonal and hexagonal faces, respectively. Along the *c* direction, neighboring Sr1- and Sr2-centered prismatic columns share faces defined by the mixed atoms (M2−M2−M2−M2), and neighboring Sr1- and Sr1-prismatic columns share the Sn4−Sn4 edges. Similar linkages occur for the LT structure, but here the mixed M2 sites become ordered Au4 and Sn1, Figure 4b. As a result, all waist-to-vertex bonds within Sr1-pentagonal and Sr2-hexagonal prisms are classified as interlayer bonds; these bonds are marked in italics in Table 4.

As to geometry variations, the complete ordering between Au and Sn in the LT structure results in an optimized structure. Although $d_{\mathrm{Au2-Au4}}$ in the LT structure is larger than its parallel bond distance $d_{\mathrm{Au1-M2}}$ in the HT structure, 3.1864(9) versus 3.027(2) Å, the LT structure generally contains more homogeneous bond distances. As given in Table 4, the mixed

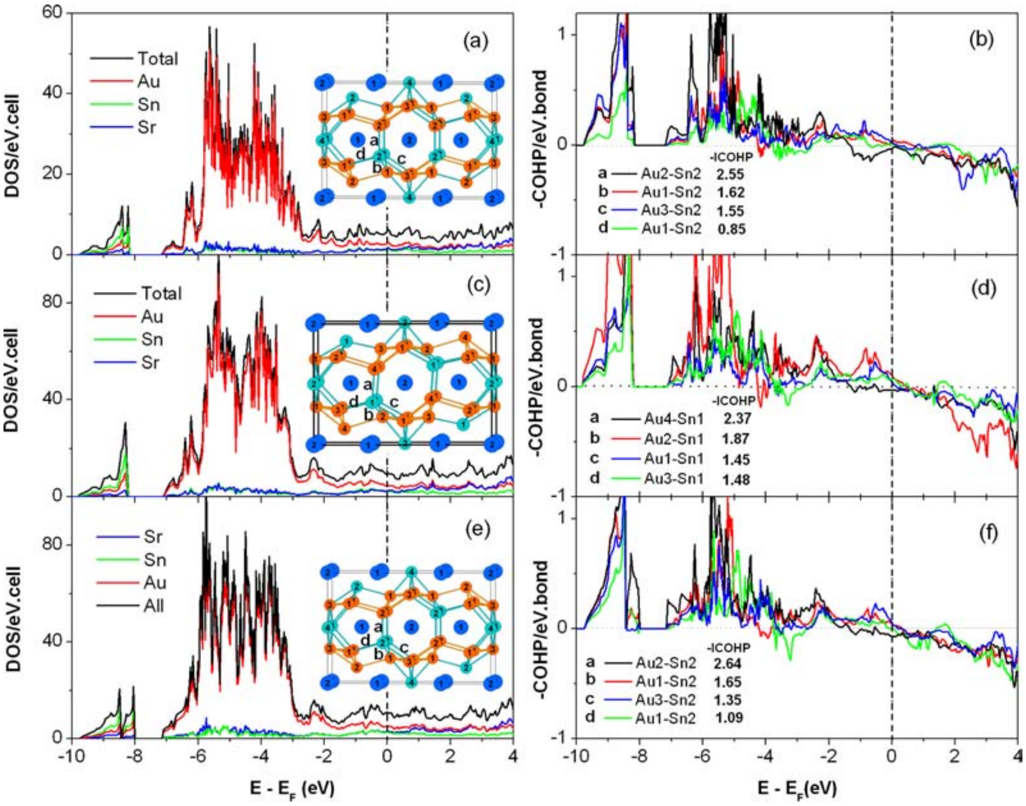

Figure 5. Density of states (DOS) and crystal orbital Hamilton population (COHP) data for selected bonds in (a, b) the energy-minimal ordered model (*I2mm*) for HT structure, (c, d) the LT structure, and (e, f) the pseudo-*Pnnm* model for the HT structure of $Sr_3Au_8Sn_3$.

M2−M2 and M2−Au1 distances in the HT structure are the shortest (2.609(3) Å) and longest bonds (3.027(2) Å) between electronegative atoms in that structure, respectively. The M2−M2 distance is about 0.45 Å less than the sum of metallic radii of Au and Sn (3.062 Å, CN = 12).[36] However, these become much more similar in the LT structure, 2.687(1) Å for Au4−Sn1 and 2.803(1) Å for Au3−Sn1 (Table 4 and Figure 3). The bond distance changes on cooling thus reflect the structural optimization driven by better chemical bonding but a change that is opposed by the accompanying decrease in entropy, below.

Bonding. Figure 5a and 5b shows the density of states (DOS) and crystal orbital Hamilton population (COHP) data for the (minimal energy) ordered *I2mm* model of the HT structure of $Sr_3Au_8Sn_3$ and in Figure 5c and 5d the DOS and COHP data for the LT structure (*Pnnm*), as well as in Figure 5e and 5f for the model with second lowest energy, which is referred as pseudo-*Pnnm* model in order to differentiate it from the true *Pnnm* model for the LT structure. These all serve to enhance energetic reasons why *Pnnm* symmetry is preferred at lower temperatures. As shown, all three models give essentially similar features in DOS patterns, which is reasonable because they all have the same composition and similar structures (see insets). However, judging from COHP data plotted (and listed) for parallel bonds, Fermi levels for both the *I2mm* (lower energy) model of the HT structure (Figure 5b) and the LT structural model (Figure 5d) are located close to energies at which bonding and antibonding interactions cross, indicating each structure is essentially optimized in terms of chemical bonding.

Although the pseudo-*Pnnm* model is less well optimized for the HT structure, parallel analyses of its COHP data and those of the LT structure (Figure 5b) allow a straightforward comparison because the differences between these two models lie only in the geometry, not atom coloring. Therefore, the four bond lengths around Sn2 in the pseudo-*Pnnm* model and Sn1 in the LT structure, at which sites disorder to order occurs, are selected for comparison. In the pseudo-*Pnnm* model, Sn2 is bonded to four neighboring Au atoms, at 2.609−3.027 Å. In comparison, parallel distances in the LT structure range from 2.687 to 2.856 Å, more homogeneous in terms of bond lengths. Since a distance of 2.609 Å is approaching the low limit of an Au−Sn bond (above), the extremely short bond requires additional energy (compared to optimized bonds) to stabilize the structure. In fact, the shortest Au2−Sn2 bond exhibits considerable antibonding interactions just below the Fermi energy (E_F), whereas the longest Au1−Sn2 bond shows antibonding interactions at about −3.0 eV and immediately above E_F, Figure 5a. In contrast, parallel bonds in the LT structure are optimized: although Au4−Sn1 remains appreciably antibonding at E_F, the integrated area for the antibonding states is 0.02/eV·bond, smaller than that for Au2−Sn2 (0.12/eV·bond). The antibonding interactions for the Au3−Sn1 bond at −3.0 eV in the LT structure are also much smaller. Meanwhile, the other two bonds with reasonable distances remain bonding interactions.

Entropy Change in the Phase Transition. One clear component in the thermodynamic differences between the LT and the HT forms is the entropy change associated with their respective order and disorder, four each Au4 and Sn1 atoms turning into eight 50:50 Au−Sn mixtures (M2) (or one-half these numbers when we consider single formula units or mole quantities since $Z = 2$). Other distortions in the transformation are numerous, but these are all associated with enthalpy changes (below). Standard statistical methods for mixing express the result as $4\sum n_i \ln n_i$ in which n_i represents the 0.50 mol fraction in our mixtures. This sum gives ΔS = 2.74 cal K^{-1} mol^{-1} at the transition temperature of 727 K, or $T\Delta S$ = ΔH = 1.99 kcal mol^{-1} for the equilibrium transformation. In contrast, DTA measurements for a 91.6 mg sample on a calibrated instrument, Figure S2, Supporting Information, yield ~2.54 kcal mol^{-1} for ΔH of the transition around 454 °C. The fact that $T\Delta S$ is smaller by a factor of ~1.3 is at least plausible inasmuch as substantial changes in bonding energies, not just disorder, accompanying LT−HT transformation. The more obvious are reflected in the distances before and after the transition that are listed in Figure 3, particularly in the pentagonal prismatic feature. The absolute distance difference in these average 0.08 Å, with the largest about twice this amount. Of course, the transition was not accomplished under reversible conditions either.

■ CONCLUSION

In summary, $Sr_3Au_8Sn_3$ was synthesized through fusing stoichiometric amount of elements at 800 °C and annealing treatments at different temperatures. This 3:11 structure, with small phase width, allows a temperature-dependent structural change from *Immm* symmetry above ~454 °C to *Pnnm* symmetry below there. These are in great contrast to the large phase breadth of a more or less analogous $CaAu_xGe_{11-x}$ (x = 7−8) which separates into two phases as the composition is changed. Bonding analyses with the aid of COHP data revealed that the present disorder-to-order structural transformation is correlated with optimization of certain chemical bonds, particularly those with extremely short distances at higher temperature.

■ ASSOCIATED CONTENT

Ⓢ Supporting Information

DTA data for $Sr_3Au_8Sn_3$; seven ordered models built from the HT structure, and data input of the *I2mm* model for LMTO calculations; CIF output. This material is available free of charge via the Internet at http://pubs.acs.org.

■ AUTHOR INFORMATION

Corresponding Author

*E-mail: jcorbett@iastate.edu.

Notes

The authors declare no competing financial interest.

■ ACKNOWLEDGMENTS

This research was supported by the U.S. National Science Foundation, Solid State Chemistry, through grant DMR-0853732. All of the research was performed in the facilities of the Ames Laboratory, U.S. Department of Energy. J.V. was a participant in the Freshman Honors Student Program at ISU.

■ REFERENCES

(1) Corbett, J. D. *Inorg. Chem.* **2010**, *49*, 13.
(2) In *Chemistry, Structure, and Bonding of Zintl Phases and Ions*; Kauzlarich, S. M., Ed.; VCH: New York, 1996.
(3) Wang, F.; Miller, G. J. *Eur. J. Inorg. Chem.* **2011**, *2011*, 3989.
(4) Pyykkö, P. *Annu. Rev. Phys. Chem.* **2012**, *63*, 45.
(5) Lin, Q.; Corbett, J. D. *Inorg. Chem.* **2008**, *47*, 7651.
(6) Lin, Q.; Corbett, J. D. *J. Am. Chem. Soc.* **2007**, *129*, 6789.
(7) Lin, Q.; Corbett, J. D. *Inorg. Chem.* **2010**, *49*, 4570.
(8) Lin, Q.; Corbett, J. D. *Inorg. Chem.* **2010**, *49*, 10436.
(9) Hume-Rothery, W. *J. Inst. Met.* **1926**, *35*, 295.
(10) Hume-Rothery, W.; Raynor, G. V. *The Structure of Metals and Alloys*, 4th ed.; Institute of Metals: London, 1962.
(11) Mizutani, U. *Hume-Rothery Rules for Structurally Complex Alloy Phases*; CRC Press: London, England, 2011.
(12) Amerioun, S.; Häussermann, U. *Inorg. Chem.* **2003**, *42*, 7782.
(13) Lin, Q.; Corbett, J. D. *Inorg. Chem.* **2009**, *48*, 5403.
(14) Stacey, T. E.; Fredrickson, D. C. *Dalton Trans.* **2012**, *41*, 7801.
(15) Tkachuk, A. V.; Mar, A. *J. Solid State Chem.* **2007**, *180*, 2298.
(16) Gout, D.; Barker, T. J.; Gourdon, O.; Miller, G. J. *Chem. Mater.* **2005**, *17*, 3661.
(17) Villars, P.; Calvert, L. D. *Pearson's Handbook of Crystallographic Data for Intermetallic Phases*, 2nd ed.; American Society of Metals: Materials Park, OH, 1991; Vol. *1*.
(18) Todorov, E.; Sevov, S. C. *J. Solid State Chem.* **2000**, *149*, 419.
(19) Grin, Y.; Ellner, M.; Hiebl, K.; Rogl, P.; Sichevich, O. M.; Myakush, O. M. *J. Alloys Compd.* **1994**, *205*, 285.
(20) Lin, Q.; Corbett, J. D. *J. Am. Chem. Soc.* **2012**, *134*, 4877.
(21) Cordier, R.; Roehr, C.; Kussmann, D.; Hoffmann, R. D.; Pöettgen, R. *Z. Anorg. Allg. Chem.* **2001**, *627*, 2053.
(22) Lin, Q.; Corbett, J. D. *Inorg. Chem.* **2011**, *50*, 1808.
(23) Hoffmann, R.-D.; Pöttgen, R.; Kußmann, D.; Niepmann, D.; Trill, H.; Mosel, B. D. *Solid State Sci.* **2002**, *4*, 481.
(24) Kraus, W.; Nolze, G. In *Powder Cell for Windows*. http://www.bam.de/de/service/publikationen/powder_cell.htm.
(25) Holland, T. J. B.; Redfer, S. A. T. *Miner. Mag.* **1997**, *61*, 65.
(26) *SHELXTL*, 6.10 ed., Bruker Analytical X-ray Systems, Inc.: Madison, WI. 2000.
(27) Gelato, L. M.; Parthé, E. *J. Appl. Crystallogr.* **1987**, *20*, 139.
(28) Andersen, O, K.; Jepsen, O. *Phys. Rev. Lett.* **1984**, *53*, 2571.
(29) Shriver, H. L. *The LMTO Method*; Springer-Verlag: Berlin, Germany, 1984.
(30) Tank, R.; Jepsen, O.; Burkhardt, A.; Andersen, O. K. *TB-LMTO-ASA Program*, Version 4.7; Max-Planck-Institut für Festkörperforschung: Stuttgart, Germany, 1994.
(31) Dronskowski, R.; Bloechl, P. E. *J. Phys. Chem.* **1993**, *97*, 8617.
(32) Feller-Kniepmeier, M.; Heumann, T. *Z. Metallkd.* **1960**, *51*, 404.
(33) Bruzzone, G. *Atti Accad. Naz. Lincei Cl. Sci. Fis. Mat. Nat. Rend.* **1970**, *48*, 235.
(34) Bärnighausen, H. *MATCH−Commun. Math. Chem* **1980**, *9*, 139.
(35) Gomes de Mesquita, A. H.; Buschow, K. H. J. *J. Alloys Compd.* **1967**, *22*, 497.
(36) Pauling, L. *The Nature of the Chemical Bond*, 3rd ed.; Cornell University Press: Ithaca, NY, 1960.